PEER REVIEWED

Preliminary Study on Low-Pressure Cold Spray Process Parameters: Effect on Mechanical and Photocatalytic Properties of TiO$_2$ Coatings

W. Seremak[1] · M. Jasiorski[1] · A. Baszczuk[1] · M. Winnicki[2]

Abstract The TiO$_2$ photocatalytic coatings' most important properties are durability and photocatalytic activity. Those features form a basis to determine its degree of usefulness. In this study, the self-synthesized amorphous TiO$_2$ powder was used for low-pressure cold spray photocatalytic coatings. Two strategies were adopted to change the surface properties, which can influence the mechanical properties of the coatings: (I) reduction of the scanning step and (II) filling the depressions in the already sprayed coating with the second layer. The coatings surface topography (measured by roughness and waviness) results showed that the first strategy makes coatings thicker, with a more uniform surface. The second strategy leads to obtaining more rough surfaces with no significant change in the thickness. The preliminary study results indicate that the first strategy was superior to the other one, in terms of both mechanical (described by cohesion and adhesion) and photocatalytic (measured by the decomposition of methylene blue under UV) properties of the coatings.

✉ W. Seremak
wioletta.seremak@pwr.edu.pl

1   Department of Mechanics, Materials and Biomedical Engineering, Wroclaw University of Science and Technology, 25 Smoluchowskiego Street, 50-370 Wroclaw, Poland

2   Department of Materials Science, Strength and Welding Technology, Wroclaw University of Science and Technology, 5 Łukasiewicza Street, 50-371 Wroclaw, Poland

Graphical Abstract
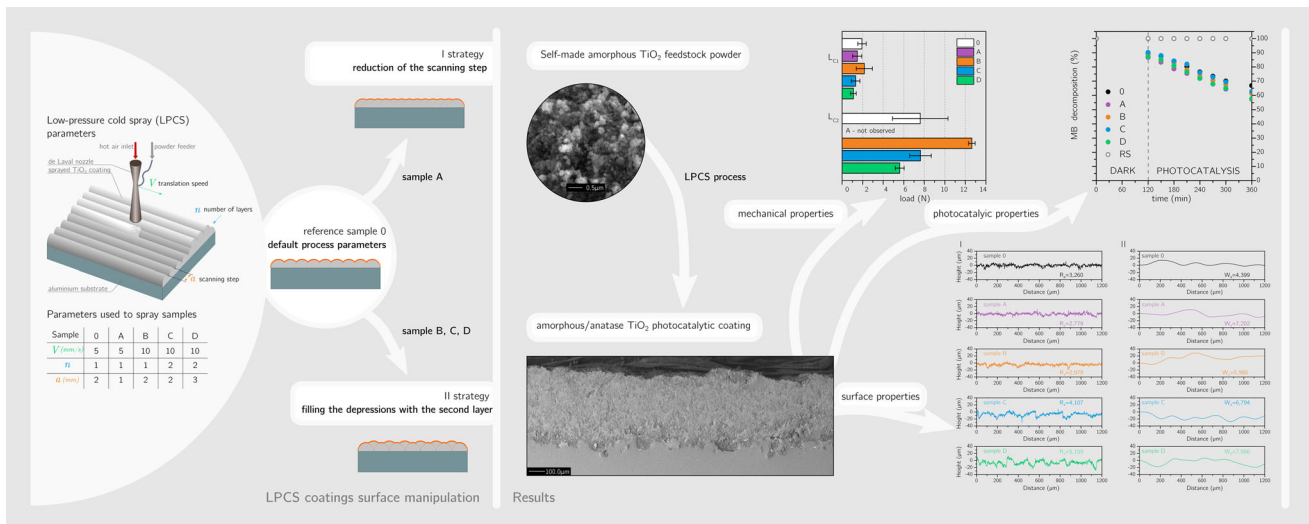
Introduction

Photocatalytic materials form the basis for ecologically clean, safe, and sustainable mineralization processes of pollutants, making use of practically unlimited solar energy. A material most frequently used for the photocatalytic process is titanium dioxide (TiO$_2$) which in different types (amorphous and crystalline structures: brookite, anatase, and rutile) and forms (powder/coating) can provide a broad range of applications (Ref 1). Two approaches are dominant among TiO$_2$ photocatalysis methods: suspensions and films/coatings. The difference between the two lies primarily in the efficiency of the photocatalytic process, which is higher in powders due to the larger surface area per unit volume (Ref 2).

However, over the last years, it became clear that TiO$_2$-based suspensions have certain limitations. Among them, the most important is its troublesome recovery from the cleaned medium, making it hard to reuse the photocatalytic powder. The filtration of nanopowders is particularly challenging (Ref 3). The incomplete separation of the nanoparticles causes the release of the photocatalyst into the aquatic environment. Due to their increasing concentration in coastal waters and the sediment, nanoscale photocatalysts can become serious post-process pollution (Ref 4). TiO$_2$ nanoparticles present in groundwater can penetrate the soil affecting its microbial function (Ref 5, 6), later taken up by plants, they enter the food chain. In this

way, TiO$_2$ nanoparticles may pose a direct threat to living organisms (by certain standards they are classified as possibly cancerogenic to humans) (Ref 7). The simplest way to control the unwanted release of the TiO$_2$ photocatalyst into the environment is to create a photocatalytic coating characterized by high mechanical properties that will guarantee its integrity while exploited.

Photocatalytic coatings are produced by various techniques, among which the low-pressure cold spray technique is known to be an economical and scalable surface engineering technique (Ref 8). In this low-temperature process, the deformation of the powder is used instead of heat (used in typical thermal spray processes) to cause consolidation of the coating material. To deform particles, the powder is accelerated above the sonic velocity and impinged on a substrate material. The low amount of heat created in the coating production process prevents uncontrolled crystallization, maintaining the initial properties of the TiO$_2$ feedstock powder (Ref 9).

However, the brittleness of TiO$_2$, typical for ceramic materials, makes the cold spray deposition problematic due to the lack of plastic deformation necessary to achieve a good level of adhesion to the substrate. The most effective remedy for this is the modification of the TiO$_2$ powder, namely the agglomeration of the particles, which facilitates its accretion when sprayed. The agglomerated nano-TiO$_2$ particles cannot deform. Still, other mechanisms can take place, such as breaking down/deformation of the whole agglomerates in certain conditions (Ref 10). Changing the deposition character of the crystalline feedstock powder from brittle to ductile reduces the amount of energy needed for powder deposition (Ref 11).

The agglomeration of the TiO_2 feedstock powder is achieved either by crystalline powder chemical modification (Ref 11, 12) or by the use of self-made amorphous feedstock powder (Ref 13), where agglomeration is a natural result of the synthesis. The latter is characterized by properties that not only facilitate its deposition process in cold spray but also make it a potential alternative to commercially available crystalline powders. When sprayed onto a substrate material, the amorphous powder partially transforms into anatase, creating a two-phase coating structure (Ref 13). The two-phase coating material can cope with the thermal gradient after the spraying process, by contrast to fully crystalline ones, where cracks induced by the fast cooling of the coating and substrate (characterized by different thermal expansion coefficients) are often present (Ref 13). Sprayed with the same process parameters, amorphous TiO_2 powder forms thicker coatings in comparison to crystalline polymorphs, such as anatase and rutile. Additionally, the adhesion of the partially amorphous cold-sprayed coatings exceeds values reported for coatings sprayed out of anatase or rutile (Ref 14). Contrary to appearances, it has been shown that as a photocatalytic material, amorphous powder has a much higher specific area, its electronic structure is similar to crystalline (Ref 15), and the abundant structural defects may contribute to the charge carrier transportation mechanism, increasing the conductivity of the material (Ref 16, 17).

Certainly, amorphous TiO_2 cold spraying is a promising subject, but not much has been reported thus far on the mechanical properties of those coatings. In the context of its future operation, the strength of the photocatalyst is of great importance since it is a deciding factor for its safe usage. As a photocatalyst, the coating should be thick, porous, and feature a large specific surface area (linked to high waviness and roughness of the surface) (Ref 18). At the same time, its strength depends on cohesion and adhesion, which are higher in dense materials (Ref 19) tightly connected to the substrate (Ref 20). Another factor that can influence the coating's strength is its surface topography. Rough surfaces are known to damage material strength (Ref 21). Hence, striving for the highest surface area possible may disqualify the photocatalyst from use. Since particles whose bonding was broken off may be swept away in the photocatalytic process and leaked into the environment.

In this preliminary study, the relation between the surface features of the cold-sprayed coatings (described by roughness) and their mechanical properties (measured by cohesion and adhesion) is researched. TiO_2 photocatalytic coatings were deposited by low-pressure cold spray (LPCS) technique using amorphous feedstock powder. The reduction of the surface roughness was completed by

changing the spraying process parameters. Two strategies were adopted to change the surface properties: (I) reduction of the scanning step and (II) filling the depressions in the already sprayed coating's surface with the second layer of cold-sprayed powder. Additionally, the methylene blue (MB) dye decomposition tests were carried out to assess the photocatalytic capabilities of the coatings. The fabricated coatings were compared to a reference sample 0 sprayed with the process parameters the same as in (Ref 14).

Materials and Methods

Synthesis of Feedstock Powder and Preparation of Coatings

The amorphous TiO_2 feedstock powder was obtained via the sol-gel method. Titanium isopropoxide, isopropanol, deionized water, and aqueous ammonia were used as starting materials in the synthesis. To obtain the TiO_2 colloids reagents were mixed in the plastic flask and stirred for 2 h (at room temperature). Afterward, the colloids were allowed to dry at room temperature and the TiO_2 powder was obtained. The synthesis process was more precisely discussed in the previous work of our team (Ref 22). After the synthesis process, TiO_2 powder was sieved to obtain particles smaller than 63 μm.

Photocatalytic TiO_2 coatings were formed on the substrates by low-pressure cold spraying using DYMET 413 unit (Obninsk Center for Powder Spraying, Obninsk, Russia). Aluminum alloy AW-1050A H14/H24 plates with dimensions of 20 × 20 × 4 mm were used as a substrate material. Before spraying, the substrate surface was degreased and grit-blasted with alumina powder (mesh 45). To spray samples, a standard circular de Laval nozzle was used (a throat and outlet diameters of 2.5 and 5 mm), supported by an aerosol powder feeder RBG 1000 D (Palas GmbH, Karlsruhe, Germany) which was connected to the beginning of the divergent part of the nozzle by silicon pipe (instead of the vibrating hopper supplied with the unit). Nitrogen pressurized to 0.1 MPa was used as the carrier gas and fed powder radially into the de Laval nozzle. The movement of the spraying gun was performed by a manipulator (BZT Maschinenbau GmbH, Leopoldshöhe, Germany). Air with a pressure of 0.5 MPa and a temperature of 600 °C was applied as a working gas, and the stand-off distance was constant and equal to 10 mm. A plan of experiments with variations of used parameters is displayed in Table 1. Sample 0 served as a reference and was sprayed with default parameters of the LPCS process established in (Ref 14). The first strategy (I) was carried out by spraying two samples with different scanning step

Table 1 Low-pressure cold spray parameters used to spray the TiO$_2$ coatings.

Sample	0 - reference	A	B	C	D
Traverse speed—V_x, mm/s	5	5	10	10	10
Number of layers—n_x	1	1	1	2	2
Scanning step—a_x, mm	2	1	2	2	3
Spraying time*—t_x, s	40	76	20	38	26

* the spraying time was calculated by multiplying the number of gun passes and sample length then divided by the traverse speed.

values (1) $a_0 = 2$ mm (reference sample 0), (2) $a_A = 1$ mm. The second strategy (II) was based on a multilayer approach. To avoid overheating of the coatings, all double-layer samples had their traverse speed increased, compared to reference sample 0. A large amount of heat might lead to major crystallization of the partially amorphous first layer and result in cracking and delamination of the coating. In this part of the experiment, three coatings were sprayed. Sample B (1) with scanning step $a_B = 2$ mm and one sprayed layer, (2) sample C with scanning step $a_C = 2$ mm and two sprayed layers shifted horizontally by 1 mm, (3) sample D with scanning step $a_D = 3$ mm and two sprayed layers shifted horizontally by 1.5 mm.

Feedstock Powder and Coatings Characterization

To evaluate the crystal structure of the feedstock powder and the coatings, the X-ray diffraction measurements were performed on an X-ray diffractometer Ultima IV (Rigaku, Japan), with Cu Kα irradiation ($\lambda = 1.5406$ Å) in the range of angles 2 theta from 5° to 90°, a step of 0.05, and exposure time 3 s per point.

Because the amorphous and crystalline phases have the same chemical composition diffractograms were used to roughly calculate the DOC (degree of crystallinity) of each sprayed sample, DOC was defined as the quotient of the area of all the crystalline peaks (CA) by the area of all the crystalline and amorphous peaks $(CA + AA)$ (Eq 1). Firstly, XRD patterns of the coatings' structure were acquired, plotted in the range 5° to 90°, and normalized. Then diffractograms were analyzed and anatase crystalline peaks, in the same scopes for each diffractogram, were integrated to receive the area referring to the crystalline share of the structure. Sample D was additionally processed to separate peaks that refer to the aluminum phase (substrate material), to prevent those areas from affecting the DOC results. Lastly, the integrals of each diffractometer were carried out and rough values of DOC were computed. All steps to quantify the DOC of the coatings have been performed in OriginPro 9 software.

$$DOC = \frac{CA}{CA + AA} \cdot 100\% \qquad (Eq\ 1)$$

The arithmetic average roughness (R_a) and waviness (W_a) of sprayed TiO$_2$ coatings surface were measured with a confocal laser microscope LEXT OLS4000 (Olympus, Tokyo, Japan). The measurements were taken perpendicularly to the spraying gun movement.

The morphology of the coatings was observed using an SEM microscope (Hitachi S-3400 N, Tokyo, Japan). The metallographic specimens were prepared by cutting the sample in the middle of its length. Afterward, the cross sections were polished without etching.

The thickness of the TiO$_2$ coatings sprayed on an aluminum substrate was determined through a non-destructive eddy current technique, with a Leptoskop 2042 apparatus (Karl Deutsch, Wuppertal, Germany), measured at 9 different points distributed over the coating surface of each specimen.

The cohesion and adhesion values of the obtained coatings were determined with a scratch tester (CSM Instruments, Micro-Scratch Tester, CSM Instruments, Peseux, Switzerland), at ambient temperature and pressure in the air. On an individual sample 4 scratches were performed, each of them 6 mm long. A Rockwell indenter (Graz, Austria) with a diameter of 100 μm (instead of the typical 200 μm) was equipped to cause more intense damage and observe critical loads sooner. The scratches were carried out with a load in the range from 30 mN to 13.36 N, with a linearly increasing loading rate of 10 (N/min) and speed of 4.5 mm/min. During the measurement, the normal force (F_N), friction coefficient (μ), and penetration depth (P_d) were recorded. Based on these parameters (F_N, μ, P_d) and identification of the characteristic loads (L_C): L_{C1}—cracking of coating, L_{C2}—characteristic chipping of coatings, L_{C3}—penetration of the coating into the substrate in the middle of the scratch, along with the cohesion of the coatings and adhesion of the coatings to the substrate were specified. The surface damage originating from the scratch tests was assessed with a polarized optical microscope that was part of the scratch tester unit.

The bandgap value (E_g) of the TiO$_2$ coatings was examined with a UV-Vis spectrophotometer equipped with a 75 mm integrating sphere (Specord 210, Analytik Jena, Jena, Germany). The spectra were registered in the range of 200-800 nm with a Spectralon® as the reference material. The Kubelka–Munk function (Eq 2) was used to convert the recorded reflectance (R) into the absorption coefficient ($F(R)$), and the Tauc's plot ($[F(R)h\upsilon]^{0.5}$ vs. $h\upsilon$) was drawn to determine the bandgap energy (E_g). The intersection between the linear fit and the photon energy (eV) axis gives the bandgap value (E_g).

$$F(R) = \frac{(1-R)^2}{2R} \qquad \text{(Eq 2)}$$

The photocatalytic activity of the coatings was evaluated through the MB dye decomposition. Firstly, the surface of all tested samples was subjected to at least 24-h UVA exposure. The MB solution used for conditioning and photocatalysis was freshly prepared ($C_M = 1 \cdot 10^{-5}$ mol/dm^3). The photocatalytic process was split into two parts: (I) DARK: samples were immersed in the dye solution in the dark for 2 hours to reach adsorption–desorption equilibrium (also referred to as the conditioning time); (II) PHOTOCATALYSIS: each reactor was exposed to UVA radiation, the decomposition process of the MB was recorded for 4 h. Additionally, to control possible changes in MB concentration during UV irradiation, a reactor containing only MB reference solution (RS) is also observed in the process. The experiment was carried out in a self-made reactor equipped with a UVA range bulb (model TL-K40W10R ACTINC) with the highest intensity at 380 nm. The distance between the photocatalyst surface and the source of irradiation was 75 mm. At such an arrangement, the UVA light intensity was measured with a standard photodiode power sensor (S120C, Thorlabs) and amounted to 110 µW. The extent of MB degradation in the solution was quantitatively estimated with a UV/VIS spectrophotometer (UV-VIS Nicolet Evolution 100, Thermo Lab) by analyzing the change in the MB absorbance peak at 663 nm. The absorbance values were converted into the dye concentration using the beforehand prepared calibration curve for the MB aqueous solution (absorbance vs. concentration). The degradation efficiency (D) was calculated by the following (Eq 3):

$$D = \frac{C_t}{C_0} \cdot 100\% \qquad \text{(Eq 3)}$$

where C_0 and C_t (both in mg L^{-1}) are the initial and remaining concentration of MB in the solution, respectively, at any irradiation time t (min). The kinetics of the photocatalytic decolorization rate of MB was determined using the Langmuir–Hinshelwood kinetics model, as given in the following (Eq 4):

$$ln\left(\frac{C_0}{C_t}\right) = k_{\text{app}}t \qquad \text{(Eq 4)}$$

The pseudo-first-order rate constant, k_{app}^{-1}, was calculated from the slope of $ln(C_0/C_t)$ versus irradiation time t.

Results

Morphology of the TiO$_2$ Feedstock Powder and Sprayed Coatings

The morphology of the sieved feedstock powder particles is presented in Fig. 1. After the sieving (Fig. 1a), the powder maintains the tendency to agglomerate into larger structures. Visible agglomerates are 200-500 µm large and oval-shaped, characterized by the developed surface (Fig. 1b). The minimal visible particle size is around 3 µm, yet still, it is the size of the agglomerate created by the primary particles in the size range of 400-600 nm (Ref 22), not the primary particle itself.

Figure 2 presents the cross section of LPCS samples. The spraying of amorphous TiO$_2$ feedstock powder results in properly coated substrate material: no cracks or voids are seen. In the coating/substrate interface high roughness of the grit-blasted aluminum is seen, despite irregularities, the surface is fully coated for all sprayed samples. The structure of the coating is composed of crystalline, sharp-edged particles embedded into an amorphous TiO$_2$ matrix. The coatings have more crystalline grains near the substrate, with increasing distance from the substrate/coating interface lower amount of crystalline grains is present.

In the sample 0 microstructure, the microporosity in the form of enclosed pores is visible (Fig. 2). The distribution of the pores is random. Sample A porosity, on the other hand, is the smallest near the interface and increased when moving to the top of the coating (Fig. 2A). Compared to sample 0, in sample A visible crystalline grains are larger. Sample B microstructure and porosity (Fig. 2B) are similar to sample 0. Sample C microstructure presents a higher amount of enclosed pores (Fig. 2C), additionally, crystalline grains are noticeably smaller compared to samples 0, A, and B. Lastly, sample D (Fig. 2D) is characterized by comparable porosity to sample 0; however, the amount and the size of the crystalline grains are smaller (especially near the coating/substrate interface). The higher-resolution images of all samples' microstructure are attached as supplementary files Figure 8-12.

Phase Analysis and DOC (Degree of Crystallinity) of the Coatings

The XRD patterns (Fig. 3) reveal that the LPCS process caused partial crystallization of the initially amorphous feedstock powder in all sprayed samples. The diffractograms of the samples show the broad hump at 25° which proves that quite a large share of the amorphous structure was maintained after spraying. The share of crystalline phase in the diffraction patterns of coatings is manifested in

Fig. 1 Morphology of the TiO$_2$ feedstock powder after sieving in magnification: (a) x1000; (b) x10 000.
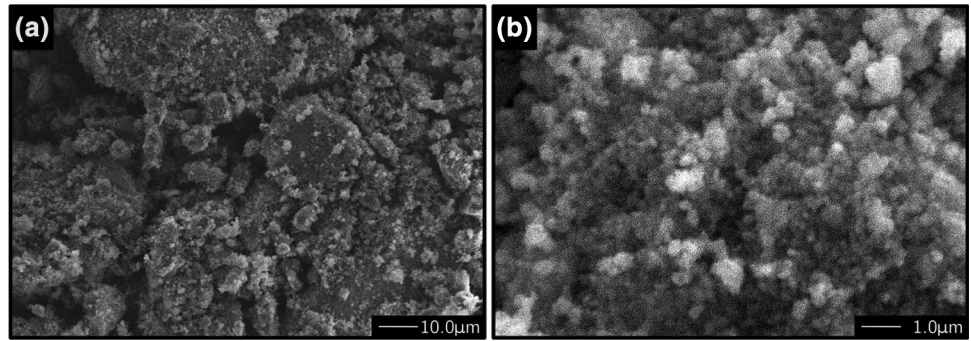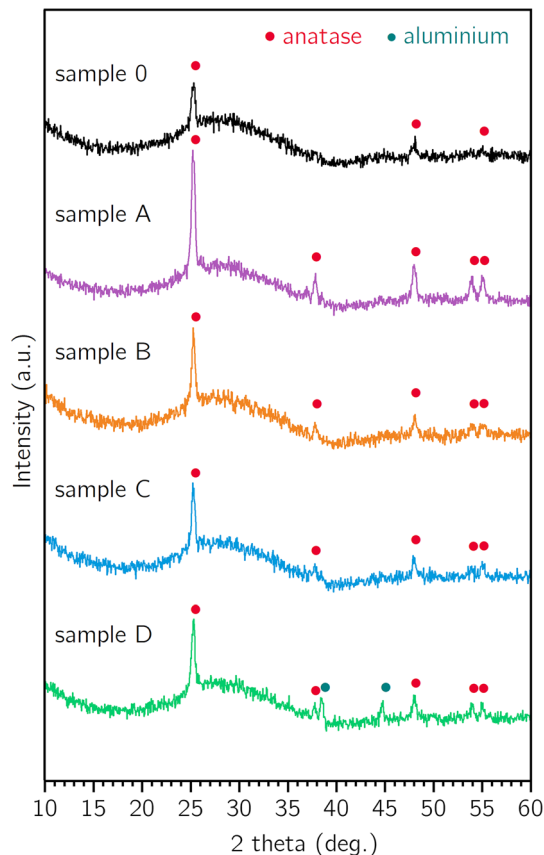

Fig. 2 SEM BSE images of the samples 0, A, B, C, and D. White arrows indicate pores, whereas black ones point to the crystalline grains in the coatings' material.
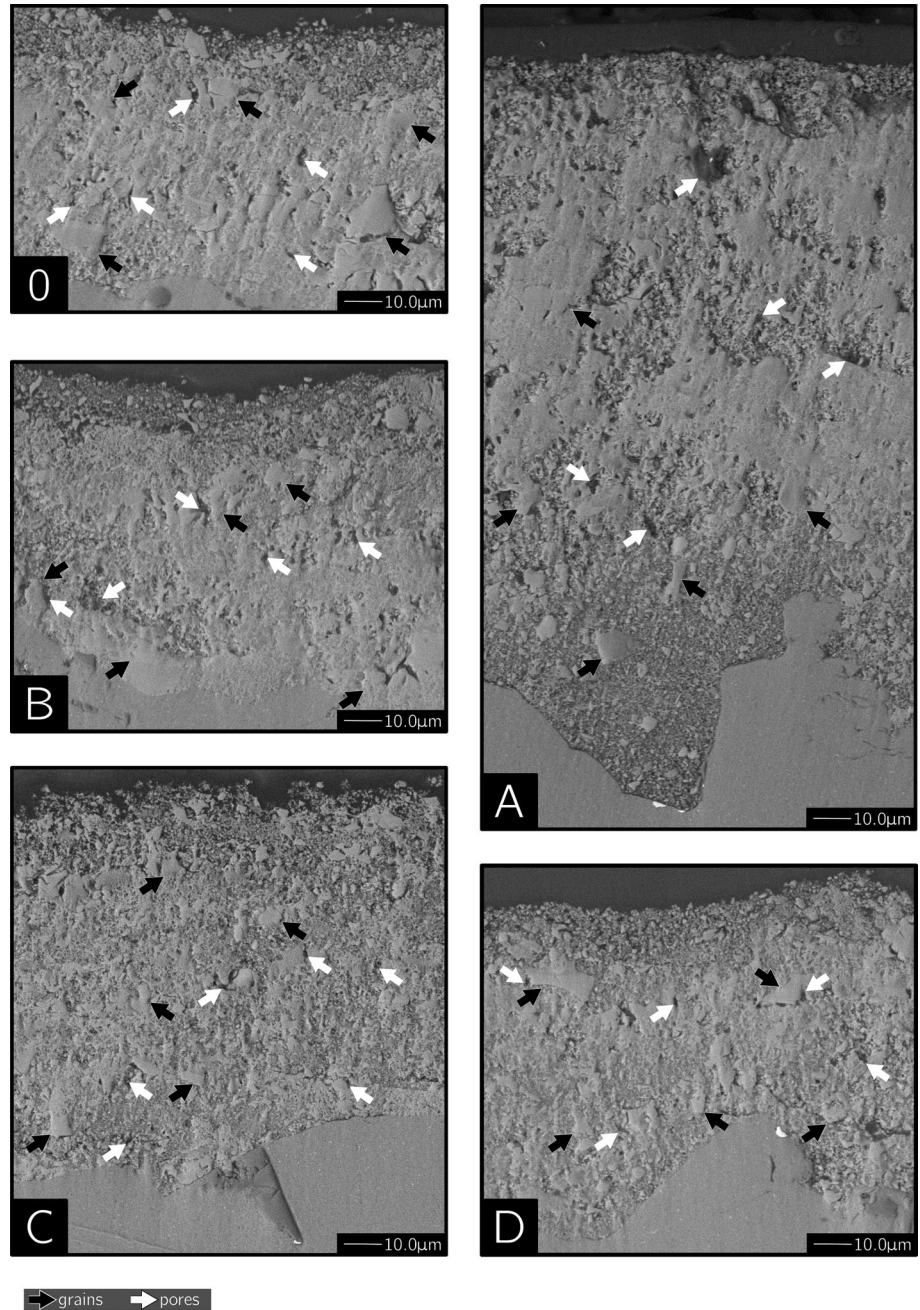
the form of diffraction peaks at 25.25°, 37.85°, 48.00°, 53.90°, and 55.05° 2 theta and corresponds to the anatase phase. Apart from identified anatase structure, the XRD pattern of sample D shows the presence of additional peaks at 38.40° 2 theta that originate from the aluminum substrate.

The crystallinity of the coating is evaluated by calculating the degree of crystallinity (DOC) of sprayed samples (Table 2). The reference sample 0 is characterized by the DOC estimated to be around 18.5%, the lowest value of all sprayed coatings. At the same time, the greatest change is observed for sample A, sprayed with reduced scanning step, and DOC rose by approximately 4%, compared to the reference sample, whereas sample B (sprayed with higher traverse velocity) and samples C and D (two-layer coatings) exhibit a negligible rise in the DOC, compared to the reference sample 0.

Surface Analysis and Thickness Measurements

To measure the apparent changes in the coatings' surface, the roughness—R_{aX} and waviness—W_{aX} of the samples were recorded and are displayed in Table 2. The R_a and W_a of the reference sample 0 are determined to be $R_{a0} = 3.260$ μm and $W_{a0} = 4.399$ μm. Sample A, where the scanning step was reduced, presents more smooth surface $R_{aA} = 2.779$ μm; however, the waviness of the surface rose to $W_{a0} = 7.202$ μm. A similar trend is observed for sample B, where traverse speed was increased, $R_{aA} = 2.979$ μm and $W_{a0} = 5.980$ μm. What's more, two-layered coatings (samples C and D), contrarily to single-layer (samples 0, A, and B) are characterized by more developed surfaces. Sample C, sprayed with scanning step $a_C = 2$ mm, is described by $R_{aC} = 4.107$ μm and $W_{aC} = 6.794$ μm. For sample D measured profile properties reached maximum values: $R_{aD} = 5.259$ μm and $W_{aD} = 7.566$ μm.

Sprayed samples are also characterized in the matter of thickness. The standard deviations of the thickness of all samples are in the same range of about 20 μm. Figure 4a illustrates the measured thicknesses of sprayed coatings. The reference sample thickness is recorded to be 80 ± 18 μm, for samples B and C similar values are registered: 90 ± 22 μm and 93 ± 23 μm. Compared to the reference sample 0, the reduction of the thickness is observed only for sample D 69 ± 18 μm; on the other

Fig. 3 XRD patterns of TiO$_2$ sprayed coatings.

Table 2 Assessed properties of the LPCS samples

Sample	0	A	B	C	D
DOC, %	18.5	22.5	19.3	19.4	19.7
R_a, μm	3.260	2.779	2.979	4.107	5.159
W_a, μm	4.399	7.202	5.980	6.794	7.566
Thickness, μm	80 ± 18	189 ± 26	90 ± 22	93 ± 23	69 ± 18
L_{c1}, N	1.9 ± 0.4	1.5 ± 0.4	2.2 ± 0.8	1.3 ± 0.4	1.1 ± 0.3
L_{c2}, N	7.6 ± 2.7	$> 13N$	12.6 ± 0.3	7.6 ± 1.0	5.6 ± 0.4
E_g value, eV	3.27	3.18	3.23	3.20	3.18
MB adsorbed in dark, %	10.6	13.3	10.2	9.8	12.7
MB decomposed in photocatalysis process, %	22.6	32.0	23.0	14.0	29.0

Fig. 4 (a) Sprayed coatings thickness, samples: 0, A, B, C, D; (b) Critical loads: L_{C1}—cohesive failure and L_{C2}—adhesive failure results acquired for samples 0, A, B, C, and D.
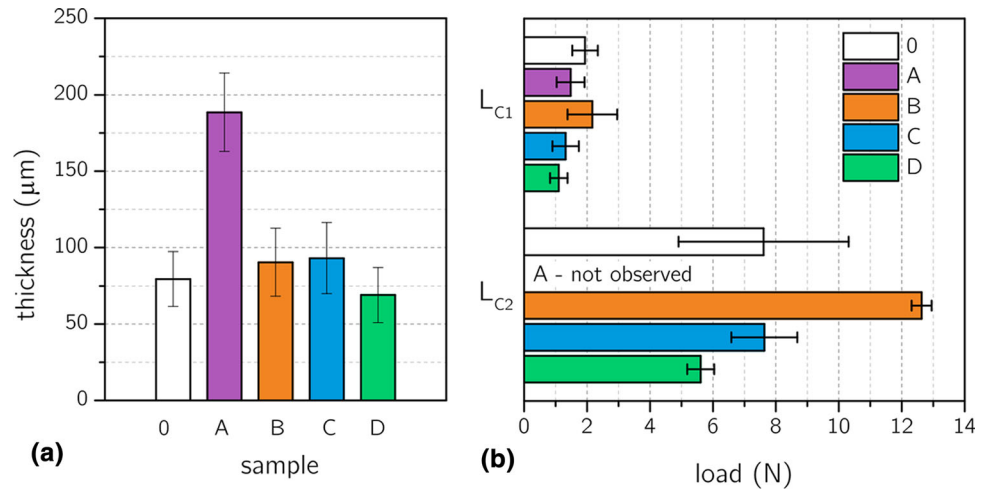
hand, sample A is two times thicker compared to reference sample 0: 189 ± 26 μm.

Cohesion and Adhesion of the Coatings

The results of the scratch tests are presented in Fig. 4b. The TiO$_2$ photocatalytic coatings are likely to work under low loads during operation, and thus, the scratches started with a 30 mN load. The critical load at which cohesive failure of samples (L_{C1}—the load at which the first crack in the coating is detected) is observed to be: 1.9 ± 0.4 N, 1.5 ± 0.4 N, 2.2 ± 0.8 N, 1.3 ± 0.4 N, and 1.1 ± 0.3 N, for 0, A, B, C, and D coating respectively. In contrast to cohesion which is similar for all tested samples, adhesion values (L_{C2}—the load at which the substrate is first exposed) are characterized by greater variation. Samples 0 and C show adhesion failure at similar load values, i.e., 7.6 ± 2.7 N and 7.6 ± 1.0 N. The deterioration of adhesive strength compared to the reference sample is observed for sample D: 5.6 ± 0.4 N. Meanwhile, samples A and B exhibit an improvement in adhesion values. Adhesive strength for sample B is 12.6 ± 0.3 N; for sample A adhesion value is estimated to be over 13.36 N since the maximum load was unable to cause the substrate material to be revealed while scratched.

Figure 5 shows optical microscopy images of surface damage at different levels of loading. In all samples, a visible trace of plastic deformation is seen right from the start (Fig. 5, left column), indicating the brittleness of the coating material. Additionally, all samples have rough surfaces and show damage in the form of chipping of the small coating's parts (marked with black arrows in Fig. 5, left column). Such damage type, observed in the range of small loads, may indicate low cohesion values. For all examined samples with the increase of the load, the same evolution of the damage type is observed: from small chipping and plastic deformation to cracking of the

coatings starting at L_{C1} (Fig. 5, middle column). Detected tensile cracks are arc-shaped and visible only in the scratch track. On further sliding, the coating material simultaneously displays two types of through-thickness cracking: ductile tensile and conformal cracking. The buckle spallation occurs at higher loads; similarly, the cracks phenomenon is visible only in the scratch area. At L_{C2} the reveal of the substrate material (white patches along the scratch in Fig. 5, right column), is first recorded. The fastest coating material removal is observed for reference sample 0. The modified samples are characterized by better adhesion of the coating material: only small bits of the substrate material are exposed (Fig. 5, left column, black arrows). For all samples, the end of each scratch track is surrounded by piled-up material, which is caused by the movement of the intender (Fig. 5, right column). And lastly, a loose coating material is present in the scratch tracks after the tests.

Optical Band Gap Determination

4Diffuse reflectance spectra of sprayed TiO$_2$ samples exhibit significant absorption in the ultraviolet region (200-380 nm). In the visible-light region (>380 nm) difference between feedstock powder and sprayed TiO$_2$ coatings is noticeable, involving the appearance of weak absorption originates from the crystallization of the TiO$_2$ amorphous structure (Fig. 6a), which is absent for the feedstock powder in this region.

The bandgaps of the TiO$_2$ samples are presented in Fig. 6b. The feedstock powder is characterized by two bandgap values of 3.56 eV and 3.42 eV. The reduction of the band gap was recorded for all sprayed coatings. Sample 0 is characterized by $E_{g0} = 3.27$ eV; samples B and C manifest $E_{gB} = 3.23$ eV, $E_{gC} = 3.20$ eV, whereas samples A and D reveal the largest decrease in the band gap value $E_{gA} = E_{gD} = 3.18$ eV. Smaller band gap values presented by sprayed samples (compared to the feedstock powder)
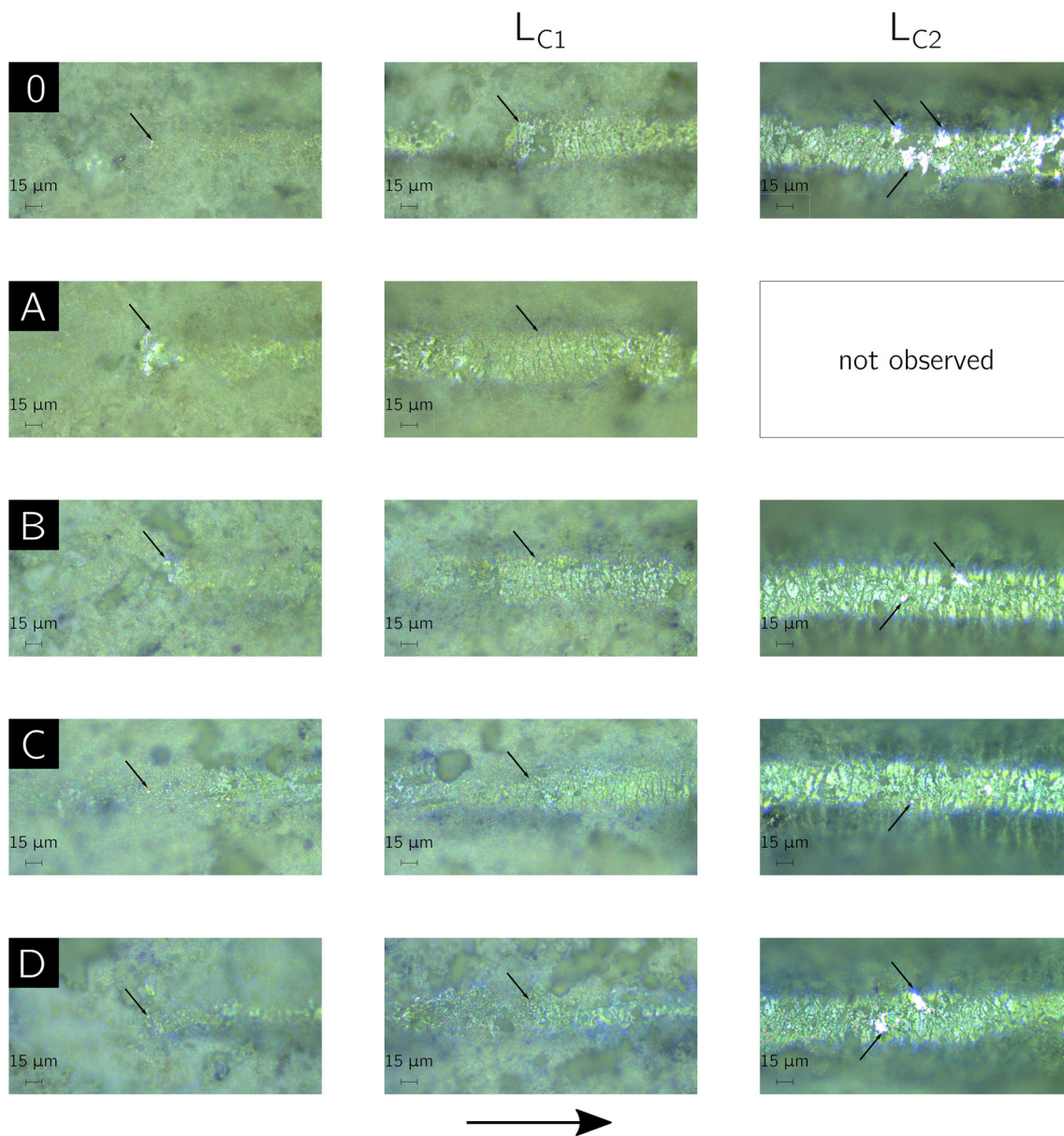
Fig. 5 Optical micrographs of the surface damage caused by scratch test of samples: 0, A, B, C, D. From left to right columns present: the damage caused by small loads, cohesive failure - L_{C1} and adhesive failure - L_{C2}. The load is progressing from left to right (following the black arrow at the bottom).

are evidence of the transformation that occurred in the structure of the TiO_2 feedstock powder, mostly referring to the crystallization of the amorphous structure (presented in Fig. 3). Minor differences between the coatings' band gap values correlate well with small differences in the degree of crystallinity.

Photocatalytic Examination

The decomposition of the MB dye was used to measure the photocatalytic properties of the coatings. Figure 7a shows the decrease in dye concentration over time. Reference sample 0, in the time of the two-hour conditioning, adsorbed 10.6% of the MB dye, and in further four-hour photocatalysis decomposed 22.6%. Meanwhile, modified samples A, B, C, and D adsorbed 13.3%, 10.2%, 9.8%, and 12.7%, and decomposed 29.3%, 27.3%, 27.6%, and 29.5%, respectively. The decomposition rate of the MB dye is higher for modified samples than for the reference sample 0, sprayed with the default process parameters. The highest adsorption rate is observed for samples A and D. Photocatalytic reaction rate constant of the photodegradation process is presented in Fig. 7b. The highest reaction rate constant achieved by sample A was 32% higher than for
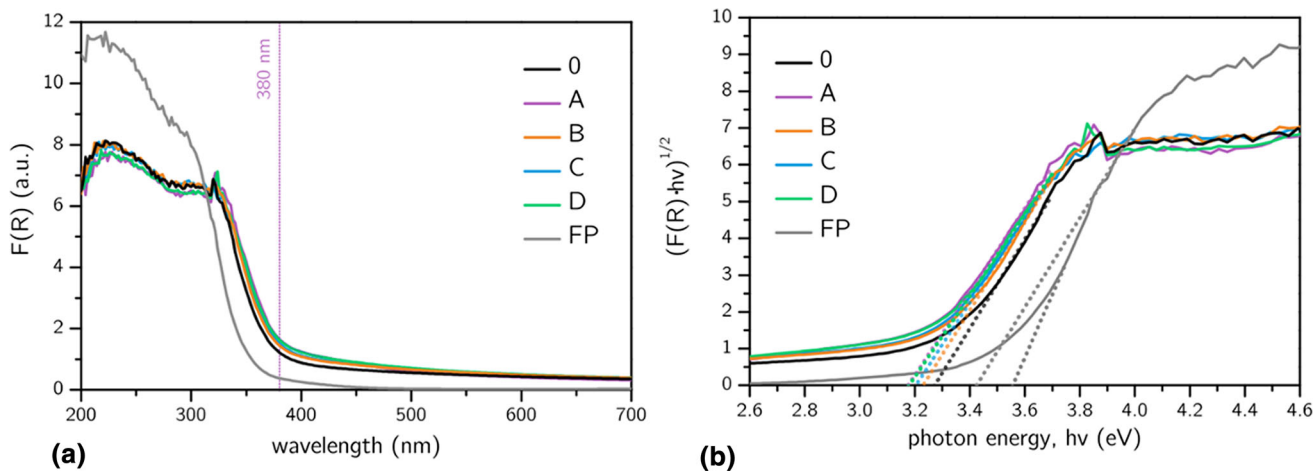
Fig. 6 (a) Kubelka–Munk function plot obtained for feedstock powder and sprayed TiO_2 coatings; (b) Tauc plots were used to determine the band gap energy values for the feedstock powder and TiO_2 coatings.
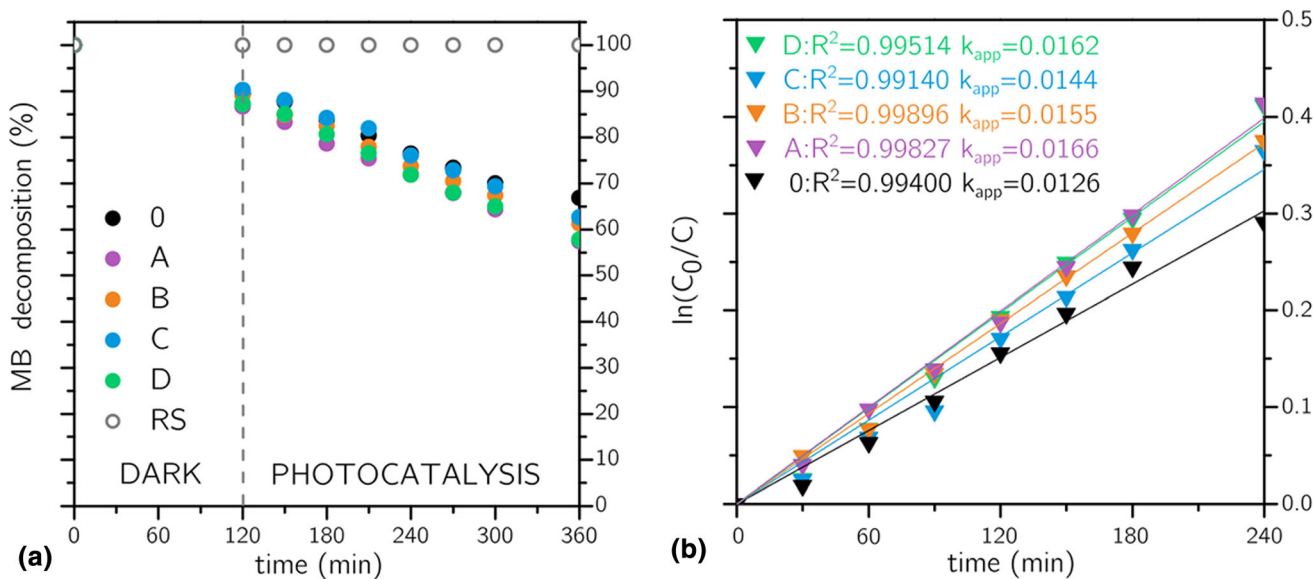
Fig. 7 (a) Adsorption and decomposition of the MB dye in the presence of samples: 0, A, B, C, D. The source of illumination was a UVA lamp. RS stands for reference solution, DARK refers to the conditioning time of the samples—carried out in the darkness, then the lamp was turned on and PHOTOCATALYSIS process was conducted; (b) pseudo-first-order kinetics and reaction rate constant for the MB photodegradation process for samples: 0, A, B, C, D.

reference sample 0. A smaller change in the photocatalytic decomposition rate, in reference to sample 0, was observed for samples D, B, and C; the decomposition rate was improved by 29%, 23%, and 14%, respectively.

Discussion

Structural and Surface Properties of the TiO_2 LPCS Coatings

The regulation of thermal energy in the low-pressure cold spray process can be done by several parameters:

(I) temperature of working gas, (II) number of layers, (III) traverse speed, and (IV) scanning step. In the present study, temperature of the working gas was constant, while the other parameters were changed. The spraying process causes the crystallization of the amorphous feedstock powder, regardless of the process' parameters choice. The amount of used thermal energy is reflected in the degree of crystallinity (DOC) of the coatings and its photocatalytic properties (Ref 23, 24). Sample A has the highest DOC which is caused by the uninterrupted spraying process. The crystallization of the sprayed TiO_2 proceeds quicker when constant heating is applied, rather than interrupted. In the same way, when comparing DOCs of samples B (constant

heating) and C (interrupted heating), no considerable difference in the crystallinity of those coatings is seen although sample C process time is almost two times longer (Table 1). A similar relationship was reported in (Ref 25), where during plasma spraying, authors reported the steady rise of the coating's average temperature resulting from the uninterrupted deposition process. Another factor responsible for sample A higher crystallinity might be the spraying time. Considering that its deposition process is the longest, sample A might have reached the highest temperature of all sprayed coatings (Ref 25). What is more, samples C and D (sprayed with different scanning step) also have similar DOCs, revealing that the scanning step has relatively less influence than the spraying time/interruptions (Ref 25) on the coatings' crystallization degree. Additionally, when looking at sample D (sprayed with the scanning step $a_D = 3$ mm) XRD patterns, besides TiO_2-phase, Al-phase peaks are recorded. Hence, to obtain continuous coatings lower values of the scanning step are needed.

The porosity of the coatings remained at a similar level despite changing the spraying process parameters. As-synthesized TiO_2 feedstock powder used in this experiment was composed of 200-500 μm agglomerates, which were built of primary particles bound together by weak attraction force. This made the feedstock powder porous even before the spraying process (Ref 26). Therefore, the porosity of the coating material was determined mostly by the properties of the feedstock powder, rather than the chosen cold spray process parameters (traverse speed, number of layers, scanning step). What is more, in all sprayed samples the most dense material was located near the coating/substrate interface. While moving from the interface to the surface of the coating, porosity and the amount of the amorphous phase in the microstructure increased. The bottom part of the coating got compressed by the following feedstock powder particles due to the plastic deformation (which is a main factor responsible for the coating build-up in the cold spray). As a result of which voids in the interface area were reduced, and the bonding between the splats was strengthened (Ref 27).

Further examination concerning the coatings' surface properties discloses that a decrease in the scanning step reduces irregularities of the coating surface (Ref 8). A decrease in sample A (sprayed with reduced scanning step) roughness compared to the reference sample 0 is seen. Similar results were achieved when cold spraying with aluminum feedstock powder; authors revealed that the flatness of the coatings was the finest when using the smallest scanning step (Ref 28). Likewise, sample B (sprayed with higher traverse speed) has its roughness slightly reduced; however, its waviness grows, compared to reference sample 0. Spraying with a higher traverse speed increases the uniformity of the sprayed particles'

distribution making the coating surface less rough (Ref 29). Samples C and D (two-layer coatings) are characterized by the highest roughness, compared to reference sample 0. The first cause of the roughness increase is the presence of undulations on the sprayed surface, resulting from a significant distance between the next sprayed beads (Ref 28). The second reason for the multilayer coatings' enhanced roughness (samples C and D) is the increased amount of gun passes (caused by spraying one layer on top of another). Alike results were observed by Kim et al. (Ref 30), where the authors manipulated the roughness of the zirconia implant surface by using a different number of deposition cycles (10, 20, and 50) in succession. The thickness and roughness gradually grew along with the number of cycles (twofold thickness increase between 10 and 50 cycles). Nevertheless, in the cited study, roughness development was desired, as it may have a positive effect on the bond between the bone and the implant surface. However, in this case, the reduction in the roughness value is favored because of its positive influence on the mechanical properties of the sample (Ref 21).

Another tendency true for all sprayed coatings is the increase of the waviness compared to the reference sample 0. In Ref 28 authors described that the waviness of coatings is mostly dependent on the particle size and velocity reached by feedstock powder. In this study, both parameters remain unchanged, and at the same time, the scanning step or the number of layers was altered, increasing the number of gun passes when sprayed. Based on the literature, such modification of the process results in thicker coatings characterized by higher waviness of the surface (Ref 31).

The thickness of sprayed coating grows with a decrease in the traverse speed (Ref 25). This trend can be observed when comparing the thickness of sample B and reference sample 0. Moreover, in samples C and D, the spraying processes differ only in the used scanning step, presenting that the material build-up rate increased with a smaller scanning step (Ref 32). Another interesting observation is that similar thicknesses were obtained for single-layer B and double-layer C samples. Despite having the same traverse speed and two times longer process time, sample C is not much thicker (Table 2). Taking into account that coatings acquired by the LPCS process are more porous in the top part of the layer (Ref 33), the attempt to spray the second layer might have resulted in the removal of loose and weak-bonded parts of the coating, preventing the material build-up.

Mechanical Properties of the TiO₂ LPCS Coatings

From the start of the scratch track, the trace after the passing intender is seen in all samples, revealing that

despite the amorphicity of the material, it is still brittle. The tensile cracks that represent the cohesive failure of all sprayed samples (observed when the fracture strength of the material is exceeded) are commonly observed in ceramic thermal sprayed coatings (Ref 19, 34). Further increase of the load causes the conformal cracking of the coating (induced by the pressing of the material into the scratch track) (Ref 35). The crispy-like character of the coatings may be caused by relatively low cohesion between sprayed TiO_2 particles. In (Ref 20) the authors described that in some cases, cold spraying is insufficient to properly bond the ceramic splats with the surrounding coating material, which was reflected by higher porosity and a decrease in the cohesion and hardness of sprayed material. Hence the cohesion values may be connected to the porosity of the TiO_2 coatings. An indirect proof of reference sample 0 porosity was presented in (Ref 36). The cold-sprayed coatings were subjected to a long-term water vapor environment. After the experiment, the passivation of the substrate was recorded, meaning that water vapor could penetrate the coating material. The cohesive strength values of the TiO_2 coatings are similar (all within the error range, Fig. 4). However, sample B distinguishes itself from the rest by slightly improved cohesion (but with the largest error range). Considering the sample B coating's surface, it seems that the higher cohesion may be ascribed not only to the surface's waviness and roughness reduction (Ref 21) but also to the smaller amount of enclosed pores in the sprayed material and the presence of large crystalline grains well-embedded into the amorphous matrix (Ref 37). The mentioned statement is also supported by the lower cohesion strength recorded for samples A, C, and D, and those coatings are characterized by both elevated roughness (samples C and D) or waviness (samples A, C, and D) as well as higher porosity (sample A in the top part of the coating) or smaller size of the crystalline grains.

The highest adhesion improvement, compared to the reference sample 0, is observed for sample A. The higher adhesion may be the result of several reasons. Firstly, in the LCPS process, it is typical to achieve more dense coatings at the base, and in sample A the material is more compressed (Fig. 2A) due to the reduced scanning step. Undoubtedly, the densified coating material could have enhanced the mechanical properties of the coating (Ref 21). Secondly, the increased thickness of the sample may have improved its resistance to damage, increasing the adhesion. Similar results were recorded by Zawischa et al. where amorphous carbon coatings (deposited by laser-induced pulsed vacuum arc technique) were investigated concerning their fracture properties (Ref 38), and by Chen et al. where authors established the influence of the plasma spraying process on cohesion/adhesion of the TiO_2 coatings (Ref 37). Additionally, the adhesive strength of the double-layer coatings (samples C and D) is inversely correlated with the scanning step values. Higher scanning step leads to spraying thinner coatings, characterized by reduced adhesive strength compared to the reference sample 0. The reason for that is the presence of less packed material with a higher amount of amorphous share near the interface observed for both samples C and D (Fig. 2C/D). The increased adhesive strength of sample B might be the result of both the higher amount of the crystalline phase near the interface (Fig. 2B) and the shortest spraying time (Table 1). Spraying thinner coating entails obtaining material with an increased compressive residual stress state at the interface and enhanced adhesion. Similarly, spraying thicker coatings or increasing the number of gun passes (samples A, C, and D) releases the stress accumulated in the interface lowering the coating substrate bond (Ref 39). Also, the adhesive strength values that characterize sprayed samples are similar to the previous results obtained in this subject (Ref 40).

Optical Properties and Photocatalytic Activity of the TiO_2 LPCS Coatings

The UV-Vis absorption spectra of the TiO_2 LPCS sprayed coatings show small absorption in the visible-light region. The apparent long tail in the visible-light region is a consequence of the lattice disorder and defects in the TiO_2 amorphous-anatase structure (Ref 41). Band gap values of the sprayed coatings (Table 2) present that all samples exhibit range of values characteristic of the TiO_2 anatase polymorph, around 3.2 eV (Ref 42). The change in optical band gap values of sprayed coatings is correlated with the crystallinity of the acquired material, resulting from different LPCS process parameters (Ref 43).

The low-pressure cold spray process has a direct impact on such properties as the DOC, thickness, and surface properties, influencing both the adsorption and the photocatalytic performance of the coatings. The MB two-hour adsorption recorded for all samples is in the same range. The highest values are observed for samples A and D. Typically the adsorption is a process driven by the coating surface area and porosity (Ref 44). Undoubtedly, the high surface area of those coatings contributes to elevated adsorption value (Ref 18) The best photocatalytic performance is observed for sample A. Longest and uninterrupted spraying time of sample A is associated with the improved crystallinity of the coating, which enhances its photocatalytic properties (Ref 45). Another sample that presents promising dye decomposition results is sample D. Described by the highest roughness and waviness proves that the specific surface area plays an important role in photocatalytic process occurrence (Ref 46).

Conclusions

In this work, we considered the connection between the chosen LPCS process parameters (scanning step, number of layers) and properties of coatings (structural, surface, mechanical, and optical), which may become a vital point to better understand and further improve LPCS photocatalytic coatings performance. The strategy based on the scanning step reduction allows spraying thicker coatings with reduced roughness. At the same time, spraying double-layer coatings results in increased roughness and waviness of the surface. The mechanical properties of the coatings measured by cohesion and adhesion values show the brittle character of amorphous/anatase TiO_2 coatings. The brittleness of the material is reflected in its relatively low cohesive strength (also arising from the porosity of the coatings) typical for ceramic coatings and observed for all samples. What is more, single-layer coatings are superior to double-layer in terms of adhesion strength. Improved adhesion is connected either to the higher thickness of the coating (obtained via a reduced scanning step), the formation of well-compressed crystalline material near the substrate-coating interface, or the presence of the residual stress in the coating/substrate interface (connected to the shorter spraying time). During the deposition, amorphous TiO_2 powder partially crystallizes to anatase. The crystallization degree can be tailored by the uninterrupted spraying process time adjustment. This way, the highest anatase share is observed for the coating sprayed with the uninterrupted, longest spraying time. Additionally, despite the mixed amorphous/anatase structure, the coatings are characterized by a band gap value the same as anatase. Photocatalytic and mechanical properties are the highest for coatings sprayed with the smallest scanning step, making it clear that the strategy based on scanning step reduction is successful. This approach not only enhanced the mechanical but also photocatalytic properties. Further improvement of the photocatalytic TiO_2 coatings might entail devising strategies that enhance the cohesion of the samples (at the same time reduce the porosity), which would make them more stable and safe when used.

Supplementary Information The online version contains supplementary material available at https://doi.org/10.1007/s11666-023-01615-0.

References

1. J. Schneider, M. Matsuoka, M. Takeuchi, J. Zhang, Y. Horiuchi, M. Anpo, and D.W. Bahnemann, Understanding TiO_2 Photocatalysis: Mechanisms and Materials, *Chem. Rev.*, 2014, **114**(19), p 9919-9986.
2. Y. Lu, S. Guan, L. Hao, and H. Yoshida, Review on the Photocatalyst Coatings of TiO_2: Fabrication by Mechanical Coating Technique and Its Application, *Coatings*, 2015, **5**(3), p 425-464.
3. H. Dong, G. Zeng, L. Tang, C. Fan, C. Zhang, X. He, and Y. He, An Overview on Limitations of TiO_2-Based Particles for Photocatalytic Degradation of Organic Pollutants and the Corresponding Countermeasures, *Water Res.*, 2015, **79**, p 128-146. https://doi.org/10.1016/j.watres.2015.04.038
4. Z. Luo, Z. Li, Z. Xie, I.M. Sokolova, L. Song, W.J.G.M. Peijnenburg, M. Hu, and Y. Wang, Rethinking Nano-TiO_2 Safety: Overview of Toxic Effects in Humans and Aquatic Animals, *Small*, 2020, **16**(36), p 1-18.
5. M. Simonin, A. Richaume, J.P. Guyonnet, A. Dubost, J.M.F. Martins, and T. Pommier, Titanium Dioxide Nanoparticles Strongly Impact Soil Microbial Function by Affecting Archaeal Nitrifiers, *Sci. Rep.*, 2016, **6**, p 1-10. https://doi.org/10.1038/srep33643
6. Z. Khan, D. Shahwar, M.K.Y. Ansari, and R. Chandel, Toxicity Assessment of Anatase (TiO_2) Nanoparticles: A Pilot Study on Stress Response Alterations and DNA Damage Studies in Lens Culinaris Medik, *Heliyon*, 2019, **5**(7), p 2069. https://doi.org/10.1016/j.heliyon.2019.e02069
7. H. Shi, R. Magaye, V. Castranova, and J. Zhao, Titanium Dioxide Nanoparticles: A Review of Current Toxicological Data, *Part. Fibre Toxicol.*, 2013, **10**(15), p 1-33.
8. S. Yin, P. Cavaliere, B. Aldwell, R. Jenkins, H. Liao, W. Li, and R. Lupoi, Cold Spray Additive Manufacturing and Repair: Fundamentals and Applications, *Addit. Manuf.*, 2018, **21**, p 628-650. https://doi.org/10.1016/j.addma.2018.04.017
9. A. Srikanth, G.M.T. Basha, and B. Venkateshwarlu, A Brief Review on Cold Spray Coating Process, *Mater. Today Proc.*, 2019, **22**, p 1390-1397.
10. M. Gardon, C. Fernández-Rodríguez, D. Garzón Sousa, J.M. Doña-Rodríguez, S. Dosta, I.G. Cano, and J.M. Guilemany, Photocatalytic Activity of Nanostructured Anatase Coatings Obtained by Cold Gas Spray, *J. Therm. Spray Technol.*, 2014, **23**(7), p 1135-1141.
11. N.T. Salim, M. Yamada, H. Nakano, K. Shima, H. Isago, and M. Fukumoto, The Effect of Post-Treatments on the Powder Morphology of Titanium Dioxide (TiO_2) Powders Synthesized for Cold Spray, *Surf. Coat. Technol.*, 2011, **206**(2-3), p 366-371.
12. A.R. Toibah, M. Sato, M. Yamada, and M. Fukumoto, Cold-Sprayed TiO_2 Coatings from Nanostructured Ceramic Agglomerated Powders, *Mater. Manuf. Process.*, 2016, **31**(11), p 1527-1534.
13. M. Winnicki, A. Baszczuk, M. Jasiorski, B. Borak, and A. Małachowska, Preliminary Studies of TiO_2 Nanopowder Deposition onto Metallic Substrate by Low Pressure Cold Spraying, *Surf. Coat. Technol.*, 2019, **371**, p 194-202.
14. M. Winnicki, L. Łatka, M. Jasiorski, and A. Baszczuk, Mechanical Properties of TiO_2 Coatings Deposited by Low Pressure Cold Spraying, *Surf. Coat. Technol.*, 2020, **2021**, p 405.

15. K. Kaur and C.V. Singh, Amorphous TiO$_2$ as a Photocatalyst for Hydrogen Production: A DFT Study of Structural and Electronic Properties, *Energy Proc.*, 2012, **29**, p 291-299. https://doi.org/10.1016/j.egypro.2012.09.035

16. V. Kavaliunas, E. Krugly, M. Sriubas, H. Mimura, G. Laukaitis, and Y. Hatanaka, Influence of Mg, Cu, and Ni Dopants on Amorphous Tio$_2$ Thin Films Photocatalytic Activity, *Materials (Basel)*, 2020, **13**(4), p 886.

17. F. Liu, X. Yan, X. Chen, L. Tian, Q. Xia, and X. Chen, Mesoporous TiO$_2$ Nanoparticles Terminated with Carbonate-like Groups: Amorphous/Crystalline Structure and Visible-Light Photocatalytic Activity, *Catal. Today*, 2016, **264**, p 243-249. https://doi.org/10.1016/j.cattod.2015.07.012

18. S. Horikoshi and N. Serpone, Can the Photocatalyst TiO$_2$ Be Incorporated into a Wastewater Treatment Method? Background and Prospects, *Catal. Today*, 2018, **2020**(340), p 334-346. https://doi.org/10.1016/j.cattod.2018.10.020

19. R. Jaworski, L. Pawlowski, F. Roudet, S. Kozerski, and F. Petit, Characterization of Mechanical Properties of Suspension Plasma Sprayed TiO$_2$ Coatings Using Scratch Test, *Surf. Coat. Technol.*, 2008, **202**(12), p 2644-2653.

20. D. Poirier, J. Legoux, R.A.L. Drew, and R. Gauvin, Consolidation of Al$_2$O$_3$/Al Nanocomposite Powder by Cold Spray, *J. Thermal Spray Tech.*, 2011, **20**, p 275-284.

21. R.S. Lima, A. Kucuk, C.C. Berndt, J. Karthikeyan, C.M. Kay, and J. Lindemann, Deposition Efficiency, Mechanical Properties and Coating Roughness in Cold-Sprayed Titanium, *J. Mater. Sci. Lett.*, 2002, **21**(21), p 1687-1689.

22. A. Baszczuk, M. Jasiorski, and M. Winnicki, Low-Temperature Transformation of Amorphous Sol-Gel TiO$_2$ Powder to Anatase During Cold Spray Deposition, *J. Therm. Spray Technol.*, 2018, **27**(8), p 1551-1562. https://doi.org/10.1007/s11666-018-0769-0

23. F.L. Toma, D. Sokolov, G. Bertrand, D. Klein, C. Coddet, and C. Meunier, Comparison of the Photocatalytic Behavior of TiO$_2$ Coatings Elaborated by Different Thermal Spraying Processes, *Proc. Int. Therm. Spray Conf.*, 2006, **15**(December), p 576-581.

24. M. Bozorgtabar, M. Rahimipour, and M. Salehi, Novel Photocatalytic TiO$_2$ Coatings Produced by HVOF Thermal Spraying Process, *Mater. Lett.*, 2010, **64**(10), p 1173-1175. https://doi.org/10.1016/j.matlet.2010.02.042

25. H. Zhang, W. Xia, G. Wang, Y. Yang, and Y. Zou, An Integrated Investigation Approach for Coating Temperature Measurement and Control during Plasma Spraying, *J. Therm. Spray Technol.*, 2008, **17**(2), p 263-274.

26. T.A. Rahim, K. Takahashi, M. Yamada, and M. Fukumoto, Effect of Powder Calcination on the Cold Spray Titanium Dioxide Coating, *Mater. Trans.*, 2016, **57**(8), p 1345-1350.

27. A.M. Vilardell, N. Cinca, A. Concustell, S. Dosta, I.G. Cano, and J.M. Guilemany, Cold Spray as an Emerging Technology for Biocompatible and Antibacterial Coatings: State of Art, *J. Mater. Sci.*, 2015, **50**, p 4441-4462. https://doi.org/10.1007/s10853-015-9013-1

28. Z. Cai, S. Deng, H. Liao, C. Zeng, and G. Montavon, The Effect of Spray Distance and Scanning Step on the Coating Thickness Uniformity in Cold Spray Process, *J. Therm. Spray Technol.*, 2014, **23**(3), p 354-362.

29. R.A. Seraj, A. Abdollah-zadeh, S. Dosta, H. Canales, H. Assadi, and I.G. Cano, The Effect of Traverse Speed on Deposition Efficiency of Cold Sprayed Stellite 21, *Surf. Coat. Technol.*, 2019, **366**(March), p 24-34.

30. H. Kim, J. Kim, and J.K. Lee, Enhancement of the Surface Roughness by Powder Spray Coating on Zirconia Substrate, *J. Nanosci. Nanotechnol.*, 2019, **19**(10), p 6285-6290.

31. M. Winnicki, T. Piwowarczyk, A. Małachowska, and A. Ambroziak, Effect of Gas Pressure and Temperature on Stereometric Properties of Al+Al$_2$O$_3$ Composite Coatings Deposited by LPCS Method, *Arch. Metall. Mater.*, 2014, **59**(3), p 879-886.

32. F.I. Trifa, G. Montavon, and C. Coddet, Model-Based Expert System for Design and Simulation of APS Coatings, *J. Therm. Spray Technol.*, 2007, **16**(1), p 128-139.

33. L. Pawlowski, *The Science and Engineering of Thermal Spray Coatings*, 2nd ed. Wiley, London, 2008.

34. A. Ghabchi, S. Sampath, K. Holmberg, and T. Varis, Damage Mechanisms and Cracking Behavior of Thermal Sprayed WC-CoCr Coating under Scratch Testing, *Wear*, 2014, **313**(1-2), p 97-105. https://doi.org/10.1016/j.wear.2014.02.017

35. S.J. Bull, Failure Mode Maps in the Thin Film Scratch Adhesion Test, *Tribol. Int.*, 1997, **30**(7), p 491-498.

36. W. Seremak, A. Baszczuk, M. Jasiorski, A. Gibas, and M. Winnicki, Photocatalytic Activity Enhancement of Low-Pressure Cold-Sprayed TiO$_2$ Coatings Induced by Long-Term Water Vapor Exposure, *J. Therm. Spray Technol.*, 2021 https://doi.org/10.1007/s11666-021-01244-5

37. H. Chen, S.W. Lee, and B.Y. Hur, Influence of Deposition Parameters on Adhesion/Cohesion of Plasma Sprayed TiO$_2$ Coatings, *Mater. Sci. Forum*, 2006, **510–511**, p 62-65.

38. M. Zawischa, S. Makowski, M. Kuczyk, and V. Weihnacht, Surface & Coatings Technology Comparison of Fracture Properties of Different Amorphous Carbon Coatings Using the Scratch Test and Indentation Failure Method, *Surf. Coat. Technol.*, 2022, **435**, p 128247. https://doi.org/10.1016/j.surfcoat.2022.128247

39. A. Moridi, S.M.H. Gangaraj, S. Vezzu, and M. Guagliano, Number of Passes and Thickness Effect on Mechanical Characteristics of Cold Spray Coating, *Proc. Eng.*, 2014, **74**, p 449-459. https://doi.org/10.1016/j.proeng.2014.06.296

40. M. Winnicki, L. Łatka, M. Jasiorski, and A. Baszczuk, Mechanical Properties of TiO$_2$ Coatings Deposited by Low Pressure Cold Spraying, *Surf. Coat. Technol.*, 2020, **405**, p 126516.

41. J.H. Pan, Z. Lei, W.I. Lee, Z. Xiong, Q. Wang, and X.S. Zhao, Mesoporous TiO$_2$ Photocatalytic Films on Stainless Steel for Water Decontamination, *Catal. Sci. Technol.*, 2012, **2**(1), p 147-155.

42. O. Ola and M.M. Maroto-Valer, Review of Material Design and Reactor Engineering on TiO$_2$ Photocatalysis for CO$_2$ Reduction, *J. Photochem. Photobiol. C Photochem. Rev.*, 2015, **24**, p 16-42. https://doi.org/10.1016/j.jphotochemrev.2015.06.001

43. J.B. Naceur, M. Gaidi, F. Bousbih, R. Mechiakh, and R. Chtourou, Annealing Effects on Microstructural and Optical Properties of Nanostructured-TiO$_2$ Thin Films Prepared by Sol-Gel Technique, *Curr. Appl. Phys.*, 2012, **12**(2), p 422-428. https://doi.org/10.1016/j.cap.2011.07.041

44. C. Fan, C. Chen, J. Wang, X. Fu, Z. Ren, G. Qian, and Z. Wang, Black Hydroxylated Titanium Dioxide Prepared via Ultrasonication with Enhanced Photocatalytic Activity, *Sci. Rep.*, 2015, **5**(1), p 1-10. https://doi.org/10.1038/SREP11712

45. S. Valencia, J.M. Marín, and G. Restrepo, Study of the Bandgap of Synthesized Titanium Dioxide Nanoparticules Using the Sol-Gel Method and a Hydrothermal Treatment, *Open Mater. Sci. J.*, 2010, **4**, p 9-14.

46. T. Jia, J. Zhang, J. Wu, D. Wang, Q. Liu, Y. Qi, B. Hu, P. He, W. Pan, and X. Qi, Synthesis Amorphous TiO$_2$ with Oxygen Vacancy as Carriers Transport Channels for Enhancing Photocatalytic Activity, *Mater. Lett.*, 2020, **265**, p 127465.